THE JOURNAL OF PHYSICAL CHEMISTRY C
A JOURNAL OF THE AMERICAN CHEMICAL SOCIETY

pubs.acs.org/JPCC Article

Adsorption of CO, H_2, H_2O, and CO_2 on Fe-, Co-, Ni-, Cu-, Pd-, and Pt-Doped $Mo_2C(101)$ Surfaces

Fan Wang, Xinxin Tian, and Haijun Jiao*

Cite This: *J. Phys. Chem. C* 2021, 125, 11419−11431 Read Online

ABSTRACT: To understand the mutual interaction and synergistic effect of transition metals and supports in heterogeneous catalysis, the less coordinated and more active surface Mo_A atoms were substituted with Fe, Co, Ni, Cu, Pd, and Pt doping atoms for investigating the adsorption of CO, H_2, H_2O, and CO_2 as well as OH, H, and O. Metal loading affects the surface electronic structure. On these surfaces, Fe, Co, Ni, Cu, and Pd doping atoms are positively charged, indicating electron transfer from the metal to the surface, while Pt doping atoms are slightly negatively charged, revealing electron transfer from the surface to the metal. On the pure surfaces and surfaces doped with four metal atoms (4M, 25%), surface Mo_A atoms are most preferred adsorption sites. By replacing all surface Mo_A atoms with eight doping atoms (8M, 50%), the more coordinated and less active surface Mo_B atoms become active. Not only surface metal atoms but also surface carbon atoms are active for the adsorption of surface species. Depending on doping metals, the adsorption of surface species can become slightly more or less exothermic. Exploring the dissociative adsorption of H_2O and CO_2 reveals metal- and loading-dependent potential energy surfaces. Full H_2O dissociative adsorption is favored thermodynamically on the 4M-doped surfaces and more exothermic than on the pure surface while doping metal-dependent on the 8M-doped surfaces. CO_2 dissociative adsorption is thermodynamically favored on the 4M-doped surfaces, while it becomes endothermic on the 8M-doped surfaces, which prefer either molecular adsorption or equilibrium between molecular and dissociative adsorption. Comparing the adsorption of CO, OH, O, and H on the pure and doped $Mo_2C(101)$ surfaces as well as the corresponding metallic low-index M(*hkl*) surfaces reveals their similarity and difference. These results provide a basis for studying the mechanisms of reactions involving these surface species.

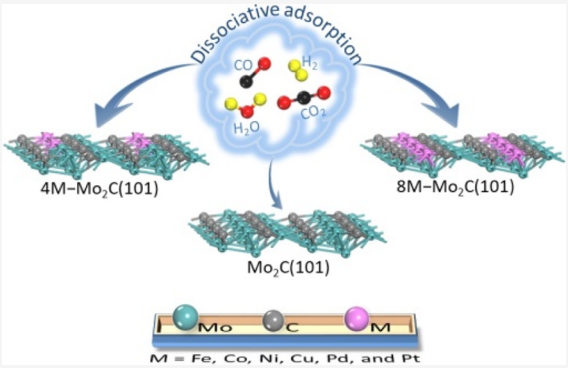

■ INTRODUCTION

In supported heterogeneous catalysis, enormous efforts have been devoted toward improving the catalytic performance by designing and controlling the loading, shape, and size of active catalysts.[1−4] However, one problem of supported catalysts is the agglomeration of metal particles during the reactions, especially at high temperatures,[5] and great attention has been paid to thermal stabilization of nanostructures. Alternatively, structurally embedded catalysts, normally embedding metal nanoparticles in an inorganic matrix or supports, have attracted great interest due to their stable catalytic activity and capacity for limiting the sintering of metal nanoparticles at high temperatures.[6]

To prepare a promising metal-atom-embedded catalyst, choosing suitable materials as matrixes (or supports) is of great significance as they could play multiple roles in specific chemical reactions. Among various supports, group IV−VI transition-metal carbides are intriguing as they possess strong interactions with doping metals and exhibit a non-negligible influence on the geometric and electronic structures of metal species.[7] As one of the most frequently studied transition-metal carbides, molybdenum carbides have been reported to have excellent catalytic activities in various chemical transformations, that is, Mo_2C-catalyzed methanol reforming gave a high H_2 yield (75%) and selectivity at 723 K.[8] In addition, ethanol decomposition to H_2 and hydrocarbons catalyzed by Mo_2C deposited on silica showed almost 100% conversion at 623−673 K.[9] Recently, Ma *et al.*[10] doped various transition metals (Pt, Fe, Co, and Ni) into molybdenum carbides by *in situ* carburization of metal-doped molybdenum oxide and found that the β-Mo_2C phase was formed in most of the cases and metal-doped molybdenum carbides showed higher methanol conversion and H_2 yield compared to pure molybdenum carbides, and Pt-doped molybdenum carbide had the highest catalytic activity and selectivity among the prepared catalysts and methanol conversion reached 100% even at a temperature

Received: April 14, 2021
Revised: May 6, 2021
Published: May 19, 2021

https://doi.org/10.1021/acs.jpcc.1c03372
J. Phys. Chem. C 2021, 125, 11419−11431

as low as 473 K and a long-time stability with a stable methanol conversion. By preparing Cu-doped molybdenum carbide ($Cu@Mo_xC_y$) catalysts from the carburization of Cu-doped molybdenum oxide, Ma *et al.*[11] found that Cu loading-dependent phase transition and these carbides ($Cu@Mo_xC_y$) exhibited promising activity for methane decomposition and long-term stability at 473−673 K. It is reported that noble metal Pt-embedded molybdenum carbides can hinder Pt sintering at high temperature and promote the interaction between Pt and molybdenum carbide,[12] and this catalyst exhibited excellent and stable catalytic activity for water-gas shift reaction at low temperature. By doping Fe and Ni into the lattice of molybdenum carbide, Wan and Leonard,[13] reported that Fe-doped β-Mo_2C are more active electrocatalysts than pure β-Mo_2C in H_2 evolution reaction, while Ni-doped β-Mo_2C are less active due to not only the electronic structure but also particle size. Very recently, Chen *et al.*[14] reported that incorporation of copper species in Mo_2C plays a crucial role in modifying the morphologic structure of Cu−Mo_2C as well as tuning the electronic state of Mo active sites, resulting in an important enhancement in the catalytic performance. They also observed a strong synergistic effect between Cu and Mo_2C in hydrogenation of dimethyl oxalate (DMO) to achieve a higher ethanol yield over the pure catalyst (67.2 vs 13.7%) at 673 K as well as excellent catalytic stability during the hydrogenation of DMO to ethanol for longer than 300 h.

Using periodic density functional theory (DFT) methods, Liu and Rodriguez[15] studied water-gas shift reaction on Mo- and C-terminated β-Mo_2C(001) surfaces. Our group studied the activation mechanisms of various intermediates on different Mo_2C surfaces.[16,17] Recently, we systematically studied the coverage-dependent adsorption structure and stability of Co, Ni, Cu, Pd, and Pt on the hexagonal Mo_2C(001) and Mo_2C(101) surfaces as well as the cubic non-polar δ-MoC(001) surface. Compared to pure Mo_2C surfaces, theoretical investigations into the structures of metal-doped molybdenum carbides are rather limited. By investigating the transition-metal-atom-embedded graphene, Krasheninnikov *et al.*[18] found that the bonding between the transition-metal atom and neighboring carbon atoms determines the magnetic and electronic properties. By substituting one surface Mo atom with one Ni atom on the Mo- and C-terminated orthorhombic Mo_2C(001) surfaces, Assary *et al.*[19] found that the Ni-doped Mo-terminated surface destabilizes the adsorption of surface O* and OH* and promotes the reaction associated with the removal of surface oxygen. Chen *et al.*[20] studied the promotion effect in water-gas shift reaction on M/MoS_2 by substituting one surface Mo atom (M = Fe, Co, Ni) and found that Ni has the largest promotion effect in reducing the effective barrier (0.72 eV), followed by Co (0.45 eV), whereas Fe has the smallest effect (0.04 eV) compared with pure MoS_2 (2.45 eV).

Since metal-doped or embedded molybdenum carbides are promising in various catalysis processes as shown above, it is interesting and worth to systematically investigate the structures of metal-doped molybdenum carbides and their adsorption properties of valuable chemical intermediates involved in various important chemical reactions. In this present study, therefore, we selected the hexagonal Mo_2C-(101) surface for doping Fe, Co, Ni, Cu, Pd, and Pt atoms at different degrees; this is because not only the hexagonal Mo_2C phase was widely detected in the preparation of metal-doped molybdenum carbide catalysts but also the (101) surface with a Mo/C = 1/1 ratio and a surface energy of 2.19 J m^{-2} was reported to be most stable.[21−23] The aim of this work is to shed light on the surface morphology and adsorption properties of these doped catalysts and provide a basis for understanding the catalytic properties of many chemical transformations involving transition-metal-doped molybdenum carbides.

■ COMPUTATIONAL METHODS AND MODELS

Methods. All calculations were performed using the plane-wave-based periodic DFT method implemented in the Vienna ab initio simulation package (VASP),[24,25] where the ionic cores are described by the projector augmented wave (PAW) method.[26] The exchange and correlation energies are computed using the Perdew, Burke, and Ernzerhof functional (PBE).[27] To achieve accurate energies with errors of less than 1 meV per atom, the cutoff energy was set at 400 eV. The Gaussian electron smearing method with σ = 0.10 eV and ISMEAR = 0 were used. Geometric optimization converged until the forces acting on the atoms were smaller than 0.02 eV $Å^{-1}$, whereas the energy threshold-defining self-consistency of the electron density was set to 10^{-4} eV. Spin polarization was included to correctly describe magnetic properties, which is essential for an accurate description of all energetic data. All transition-state structures were optimized by using the climbing image nudged elastic band method,[28] and the frequency analysis was also processed to verify an authentic transition state having only one imaginary frequency. For bulk optimization, the lattice parameters for the hexagonal Mo_2C phase are determined by minimizing the total energy of the unit cell by using a conjugated gradient algorithm to relax the ions, and a 5 × 5 × 5 Monkhorst−Pack *k*-point grid[29] is used for sampling the Brillouin zone.

Models. Generally, Mo_2C has orthorhombic[30] and hexagonal[31,32] crystalline phases. In this work, we used the hexagonal phase with an eclipsed configuration as the unit cell.[16,17,21,33] The calculated lattice parameters of the unit cell are $2a$ = 6.079, $2b$ = 6.073, and c = 4.722 Å, in good agreement with the experimental values (a = b = 3.002, c = 4.724 Å).[34] Among all hexagonal Mo_2C surfaces, the (101) surface with a Mo/C = 1/1 ratio and a surface energy of 2.19 J/m^2 was reported to be most stable.[21−23,35] Hence, we used Mo_2C(101) to execute our study, and it was modeled by a periodic slab with $p(2 \times 2)$ super cells having a surface area of 14.2 Å × 12.1 Å. We applied a four-layer model with the top two layers relaxed and the bottom two layers fixed in their bulk positions. The vacuum layer between the periodically repeated slabs was set at 15 Å to avoid significant interactions between slabs. Surface structural relaxation and total energy calculations were performed with 3 × 3 × 1 Monkhorst−Pack *k*-point sampling. For the relevant gas-phase species, we used a cubic box with a side length of 10 Å to calculate the structures and total energies.

The adsorption energy (E_{ads}) is defined according to $E_{ads} = E(X/slab) - [E(X) + E(slab)]$, where $E(X/slab)$ is the total energy of the slab with one X molecule, $E(slab)$ is the total energy of the bare slab, and $E(X)$ is the total energy of a free X molecule in the gas phase, and therefore, the more negative the E_{ads}, the stronger the adsorption. For the adsorption of atomic H or O, half of the total energy of gas-phase molecular H_2 or O_2 was used. The barrier (E_a) and reaction energy (ΔE_r) are calculated according to $E_a = E_{TS} - E_{IS}$ and $\Delta E_r = E_{FS} - E_{IS}$, where E_{IS}, E_{FS}, and E_{TS} are the energies of the corresponding

https://doi.org/10.1021/acs.jpcc.1c03372
J. Phys. Chem. C 2021, 125, 11419−11431

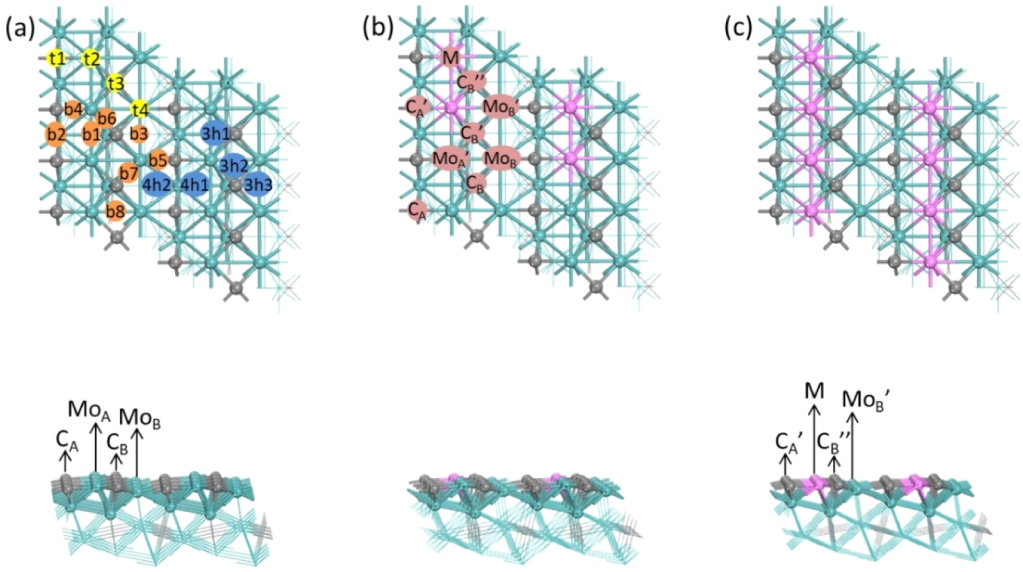

Figure 1. Top (top) and side (bottom) views of the (a) $Mo_2C(101)$, (b) 4M−$Mo_2C(101)$, and (c) 8M−$Mo_2C(101)$ surface structures and possible adsorption sites (**t**: top, **b**: bridge, **3h**: threefold hollow, and **4h**: fourfold hollow sites; C: gray, Mo: cyan, M: pink).

initial state (IS), final state (FS), and transition state (TS), respectively. All reported energetic data included zero-point energy (ZPE) correction through processing the frequency analysis. In our previous work, we used PBE to compute the high coverage adsorption and desorption of CO on the orthorhombic $Mo_2C(100)$ surface[36] and the hexagonal eclipsed $Mo_2C(001)$ surface[37] and found that the estimated desorption temperatures agree with the experimental values, and this in turn validates the PBE functional and also the calculated adsorption energies. The same is also found for the high coverage co-adsorption of CO and H_2 on the CdI_2-antitype metallic $Mo_2C(001)$ surface.[38] On the contrary, the computed adsorption energies including dispersion correction[39] are in the range of 0.25−0.54 eV stronger than those from only PBE and should be overestimated. Therefore, we used only PBE for energy calculations.

Figure 1 shows the top and side views of the $Mo_2C(101)$, 4M−$Mo_2C(101)$, and 8M−$Mo_2C(101)$ surfaces. For Mo_2C-(101), there are totally 16 surface Mo and 16 surface C atoms. Four types of surface atoms with different coordination patterns are exposed. The surface C_A atom interacts with four Mo atoms and has two dangling bonds (saturated bulk Mo coordinating with three C atoms), and the surface C_B atom interacts with five Mo atoms and has one dangling bond. The surface Mo_A atom interacts with seven Mo atoms, and the surface Mo_B atom interacts with eight Mo atoms. These four different surface atoms build four top sites (**t1**−**t4**), eight bridge sites (**b1**−**b8**), three threefold hollow sites (**3h1**−**3h3**), and two fourfold hollow sites (**4h1** and **4h2**) for adsorption. The **t1**−**t4** sites are on the C_A, Mo_A, C_B, and Mo_B, respectively. The **b1** (Mo_A−Mo_A) site has two Mo_A atoms; the **b2** (C_A−C_A) site has two C_A atoms; the **b3** (Mo_B−Mo_B) site has two Mo_B atoms; the **b4** (Mo_A−C_A) site has one Mo_A atom and one C_A atom; the **b5** (Mo_B−C_A) site has one Mo_B atom and one C_A atom; the **b6** (Mo_A−C_B) site has one C_B atom and one Mo_A atom; the **b7** (Mo_B−C_B) site has one C_B atom and one Mo_B atom; the **b8** (Mo_A−Mo_B) site has one Mo_A atom and one Mo_B atom. The **3h1** ($2Mo_A$−C_B) site has two Mo_A atoms and one C_B atom; the **3h2** (Mo_A−Mo_B−C_B) site has one Mo_A atom, one Mo_B atom, and one C_B atom; and the **3h3** ($2Mo_B$−C_B) site has two Mo_B atoms and one C_B atom. The **4h1** ($2Mo_A$−$2C_A$) site has two Mo_A atoms and two C_A atoms, while the **4h2** ($2Mo_B$−$2C_A$) site has two Mo_B atoms and two C_A atoms. The total supercell contains a $Mo_{64}C_{32}$ unit.

The 4M−$Mo_2C(101)$ surface, formed by substituting 4 surface Mo_A atoms on the pure $Mo_2C(101)$ surface with 4 doping metal atoms, has 12 surface Mo, 4 doping metal, and 16 surface C atoms. As shown in Figure 1b, nine types of surface atoms can be recognized with different coordination environments. The surface M atom interacts with six Mo atoms and one M atom. The surface C_A atom interacts with four Mo atoms; surface C_A' interacts with three Mo atoms and one M atom; the surface C_B atom interacts with five Mo atoms; the surface C_B' atom interacts with four Mo atoms and one M atom; the surface C_B'' atom interacts with three Mo atoms and two M atoms. Surface Mo_A' interacts with six Mo atoms and one M atom; the surface Mo_B atom interacts with eight Mo atoms; the surface Mo_B' atom interacts with seven Mo atoms and one M atom.

On the 8M−$Mo_2C(101)$ surface (Figure 1c), all surface Mo_A atoms on the pure $Mo_2C(101)$ surface are replaced with doping metal atoms. Therefore, this surface has totally 8 surface Mo_B atoms, 8 surface doping M atoms, and 16 surface C atoms. There are four types of surface atoms with different coordination environments. The surface M atom interacts with five Mo and two M atoms. Surface C_A' interacts with three Mo atoms and one M atom, the surface C_B'' atom interacts with three Mo and two M atoms, and the surface Mo_B' atom interacts with seven Mo atoms and one M atom.

■ RESULTS AND DISCUSSION

Since doping metals have different electronic configurations, it is meaningful to investigate the changes in geometric, electronic, and adsorption properties with the respect of catalysis. At first, we analyzed the projected density of states (PDOS) of the d-orbitals of all these doped surfaces. We compared our results with those reported previously[40] and found good accordance. On pure $Mo_2C(101)$, the PDOS shows that the d-orbitals of Mo_A with sevenfold coordination is closer to the Fermi level than Mo_B with eightfold coordination

https://doi.org/10.1021/acs.jpcc.1c03372
J. Phys. Chem. C 2021, 125, 11419−11431

Table 1. Average Bader Charge for Surface Metal Atoms on Pure $Mo_2C(101)$, 4M−$Mo_2C(101)$, and 8M−$Mo_2C(101)$ (M = Fe, Co, Ni, Cu, Pd, and Pt)

		4M−$Mo_2C(101)$						8M−$Mo_2C(101)$					
site	$Mo_2C(101)$	Fe	Co	Ni	Cu	Pd	Pt	Fe	Co	Ni	Cu	Pd	Pt
Mo_A[a]	0.79	0.85	0.88	0.89	0.88	0.91	0.91						
Mo_B[b]	0.89	0.86	0.86	0.87	0.89	0.90	0.90	0.86	0.85	0.90	0.93	0.93	0.92
C_A	−1.14	−1.13	−1.12	−1.12	−1.13	−1.10	−1.08	−1.10	−1.08	−1.06	−1.10	−1.02	−0.99
C_B	−1.32	−1.29	−1.25	−1.24	−1.25	−1.20	−1.17	−1.23	−1.14	−1.12	−1.16	−1.03	−0.98
M		0.51	0.32	0.27	0.33	0.04	−0.12	0.54	0.36	0.27	0.37	0.10	−0.03

[a]Average Bader charge of surface Mo_A' atoms in 4M−$Mo_2C(101)$. [b]Average Bader charge of surface Mo_B and Mo_B' atoms in 4M−$Mo_2C(101)$ or surface Mo_B' atoms in 8M−$Mo_2C(101)$.

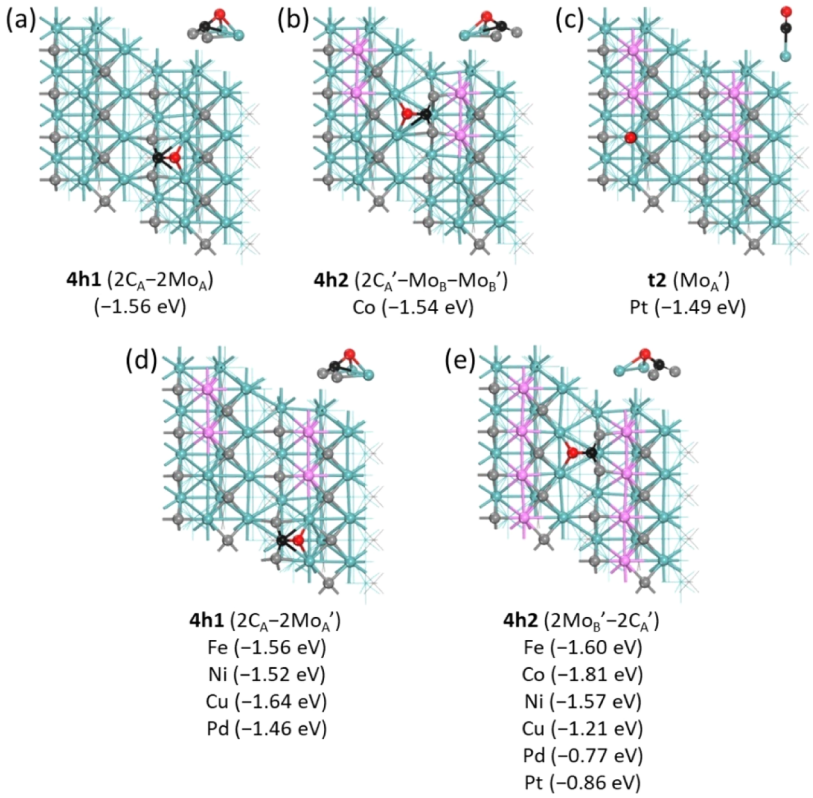

Figure 2. Most stable adsorption configurations and energies (in parentheses) of CO on (a) pure $Mo_2C(101)$, (b−d) 4M−$Mo_2C(101)$, and (e) 8M−$Mo_2C(101)$ (M = Fe, Co, Ni, Cu, Pd, and Pt; O: red, C in CO: black, C in Mo_2C: gray, Mo: cyan, M: pink).

and surface Mo_A atoms are more active than Mo_B atoms. For 8M−$Mo_2C(101)$, with all surface Mo_A atoms replaced with doping metals (Figure S1), surface Mo_B has no obvious change in PDOS, while the PDOSs of Fe and Co are closer to the Fermi level compared to those of Ni, Cu, Pd, and Pt. The same situation has also been found on the fourM−$Mo_2C(101)$ surfaces (Figure S2).

In addition to PDOS, we have analyzed the electronic effect (Bader charge analysis[41]) of different doping metals (Table 1). On pure $Mo_2C(101)$, both Mo_A and Mo_B are positively charged. On both 4M−$Mo_2C(101)$ and 8M−$Mo_2C(101)$ for 3d metals, the positive Bader charge of the doping metal is in the order of Fe (0.51) > Cu (0.33) ≈ Co (0.32) > Ni (0.27) and Fe (0.54) > Cu (0.37) ≈ Co (0.36) > Ni (0.27), respectively, in line with the order of the Allen electronegativity of Fe (1.80) < Co (1.84) ≈ Cu (1.85) < Ni (1.88).[42] Comparatively, Pd atoms are slightly positively charged for 4M− and 8M−$Mo_2C(101)$ (0.04 and 0.10, respectively), while Pt atoms are slightly negatively charged (−0.12 and −0.03, respectively), although the electronegativities of Pd and Pt are 1.59 and 1.72, respectively. The difference among Ni, Pd, and Pt might be associated with their different electronic configurations, that is, $3d^84s^2$ for Ni, $4d^{10}5s^0$ for Pd, and $5d^96s^1$ for Pt. In all cases, surface C_A and C_B are negatively charged due to the much larger electronegativity (2.544), and C_A is more negatively charged than C_B. However, both C_A and C_B become less negatively charged upon transition-metal doping, and the largest change is C_B on the 8M-doped surface. That the doped Cu atoms are positively charged agrees with the X-ray photoelectron spectroscopy analysis,[11] and these positively charged Cu species could result in high activity for methanol conversion and high stability, which might result from the strong interaction between Cu and the Mo_2C support. Having these results in hand, we computed the adsorption properties of CO, H_2O, H_2, and CO_2.

CO Adsorption. First, we studied CO adsorption. Figure 2 shows the most stable adsorption configurations, while the less stable adsorption configurations are given in Figure S3. On

https://doi.org/10.1021/acs.jpcc.1c03372
J. Phys. Chem. C 2021, 125, 11419−11431

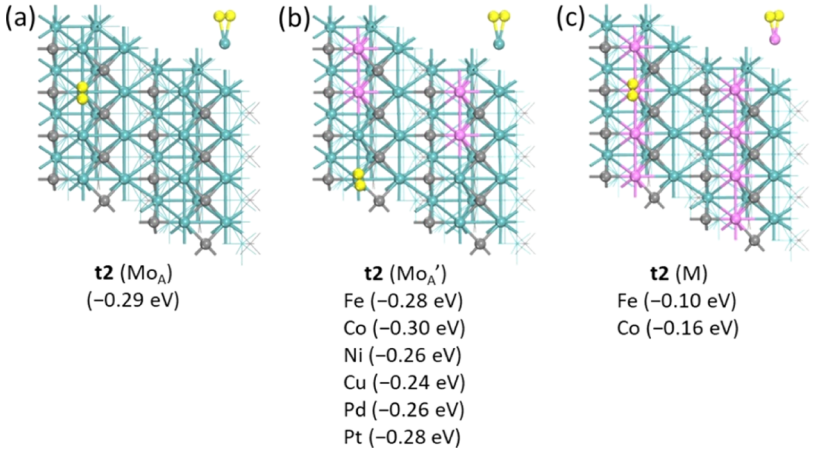

Figure 3. Most stable adsorption configurations and energies (in parentheses) of H_2 on (a) pure $Mo_2C(101)$, (b) 4M−$Mo_2C(101)$, and (c) 8M−$Mo_2C(101)$ (M = Fe, Co, Ni, Cu, Pd, and Pt; H: yellow, C: gray, Mo: cyan, M: pink).

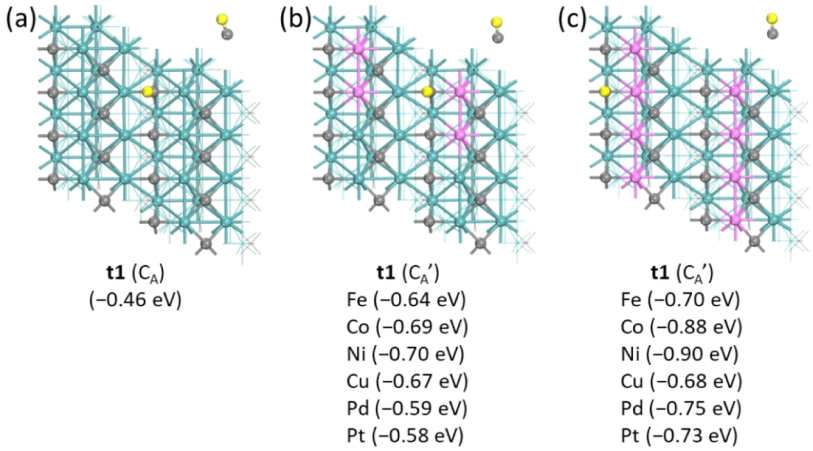

Figure 4. Most stable adsorption configurations and energies (in parentheses) of H on (a) pure $Mo_2C(101)$, (b) 4M−$Mo_2C(101)$, and (c) 8M−$Mo_2C(101)$ (M = Fe, Co, Ni, Cu, Pd, and Pt; H: yellow, C: gray, Mo: cyan, M: pink; using gaseous H_2 as a reference).

pure $Mo_2C(101)$, CO prefers the **4h1** ($2C_A$−$2Mo_A$) site with the strongest adsorption energy of −1.56 eV, followed by the **t2** (Mo_A) site (−1.53 eV), indicating their competition, while the **t4** (Mo_B) and **4h2** ($2C_A$−$2Mo_B$) sites have much lower adsorption energies (−0.96 and −0.67 eV, respectively, Figure S3). At the **4h1** site ($2C_A$−$2Mo_A$), the C atom of CO interacts with two surface C_A atoms and the O atom interacts with two surface Mo_A atoms. At the **4h2** ($2C_A$−$2Mo_B$) site, the C atom of CO interacts with two surface C_A atoms and the O atom interacts with two surface Mo_B atoms. The stronger adsorption at **4h1** than at **4h2** shows that Mo_A is more active than Mo_B. These results match well with those reported previously.[16,37]

On 4M−$Mo_2C(101)$, where half surface Mo_A atoms on $Mo_2C(101)$ are replaced with doping metals, CO prefers the **4h1** ($2C_A$−$2Mo_A'$) site for M = Fe, Ni, Cu, and Pd with adsorption energies of −1.56, −1.52, −1.64, and −1.46 eV, respectively. For M = Co and Pt, CO prefers the **4h2** ($2C_A'$−Mo_B−Mo_B') and **t2** (Mo_A') sites with adsorption energies of −1.54 and −1.49 eV, respectively, while the **4h1** ($2C_A$−$2Mo_A'$) site has lower adsorption energies (−1.45 and −1.42 eV, respectively). It is noted that CO adsorption at the top site of doping metal **t2** (M) at the **t4** (Mo_B') site and at the **4h1** (2M−$2C_A'$) site (vertically at the $2C_A'$ bridge site) for Pd and Pt is less or much less stable (Figure S3). This shows that the doping metal does not significantly affect CO adsorption at the **4h1** ($2C_A$−$2Mo_A'$) site but increases CO adsorption energy at the **4h2** ($2C_A'$−Mo_B−Mo_B') and **t2** (Mo_A') sites. However, CO adsorption around the doping metal is not competitive and favorable.

On 8M−$Mo_2C(101)$, CO prefers the **4h2** ($2Mo_B'$−$2C_A'$) site for M = Fe, Co, Ni, Cu, and Pt with adsorption energies of −1.60, −1.81, −1.57, −1.21, and −0.86 eV, respectively. For M = Pd, both **4h2** ($2Mo_B'$−$2C_A'$) and **t4** (Mo_B') sites have the same CO adsorption energy (−0.77 eV). On the contrary, CO adsorption at the top site of doping metal **t2** (M), at the **t4** (Mo_B') site, and at the **4h1** (2M−$2C_A$) site is less or much less stable (Figure S3). This shows that the doping metal promotes CO adsorption at the **4h2** ($2Mo_B'$−$2C_A'$) site, while CO adsorption around the doping metal is not competitive and favorable.

In addition to the adsorption configurations and energies, we computed CO stretching frequencies (Table S1). It is found that CO stretching frequencies at fourfold hollow sites are in the range of 1000−1300 cm^{-1}, while those at the top sites are in the range of 1900−2100 cm^{-1}. However, CO stretching frequency does not correlate with the adsorption energy since CO has close adsorption energy at fourfold hollow and top sites, that is, at **4h1** ($2C_A$−$2Mo_A$) and **t2** (Mo_A) sites on pure $Mo_2C(101)$ (−1.56 and −1.53 eV, respectively), at **4h1** ($2C_A$−$2Mo_A'$) and **t2** (M) sites on 4Fe−$Mo_2C(101)$ (−1.56

https://doi.org/10.1021/acs.jpcc.1c03372
J. Phys. Chem. C 2021, 125, 11419−11431

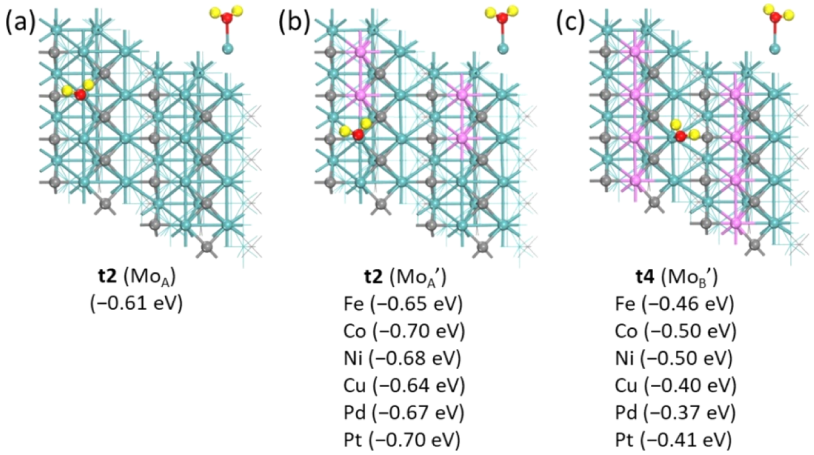

Figure 5. Most stable adsorption configurations and energies (in parentheses) of H_2O on (a) pure $Mo_2C(101)$, (b) 4M−$Mo_2C(101)$, and (c) 8M−$Mo_2C(101)$ (M = Fe, Co, Ni, Cu, Pd, and Pt; H: yellow, O: red, C: gray, Mo: cyan, M: pink).

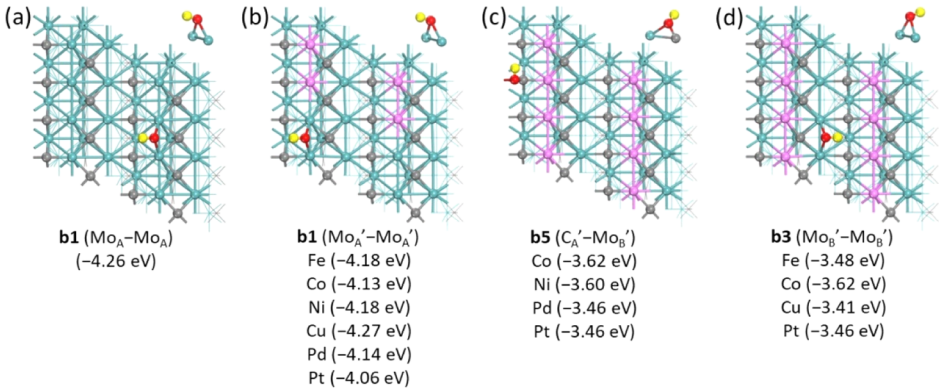

Figure 6. Most stable adsorption configurations and energies (in parentheses) of OH on (a) pure $Mo_2C(101)$, (b) 4M−$Mo_2C(101)$, and (c,d) 8M−$Mo_2C(101)$ (M = Fe, Co, Ni, Cu, Pd, and Pt; H: yellow, O: red, C: gray, Mo: cyan, M: pink).

and −1.55 eV, respectively), and at **4h2** (2Mo$_B$′−2C$_A$′) and **t4** (Mo$_B$′) sites on 8Pd−$Mo_2C(101)$ (−0.77 and −0.77 eV, respectively). These results should provide theoretical reference for assigning specific adsorption sites with the corresponding stretching frequencies.

Hydrogen Adsorption. As reported previously,[29] molecular H_2 can occupy the top site of the surface Mo atom vertically and horizontally, and the former is slightly more stable than the latter; thus, we only considered the vertical type in the present study.

On pure $Mo_2C(101)$ (Figure 3a), H_2 adsorption at the **t2** (Mo$_A$) site is exothermic (−0.29 eV), while at the **t4** (Mo$_B$) site, it is endothermic (0.13 eV) (Figure S4). On 4M−$Mo_2C(101)$, H_2 prefers the **t2** (Mo$_A$′) site with adsorption energies of −0.28, −0.30, −0.26, −0.24, −0.26, and −0.28 eV for M = Fe, Co, Ni, Cu, Pd, and Pt, respectively (Figure 3b), close to that on the pure surface. On the contrary, H_2 adsorption at the **t2** (M) site has either very low or negligible adsorption energy (Figure S4). On the **t4** (Mo$_B$ or Mo$_B$′) sites, H_2 has adsorption energies close to 0 (Figure S4). These show that on 4M−$Mo_2C(101)$, the doping metal does not significantly affect H_2 adsorption at the **t2** (Mo$_A$′) site, and H_2 adsorption around the doping metal is not favored and competitive. On 8M−$Mo_2C(101)$, H_2 adsorption at the **t2** (M) site has very low adsorption energies (−0.10 and −0.16 eV, respectively) for M = Fe and Co (Figure 3c) and negligible adsorption energy for M = Ni, Cu, Pd, and Pt (Figure S4), indicating the complete suppression of H_2 adsorption.

As H_2 prefers dissociation adsorption (−0.92 eV) on the pure $Mo_2C(101)$ surface with a very low barrier (0.31 eV),[16] we computed the adsorption of a H atom for H_2 dissociative adsorption. The most stable adsorption configurations are listed in the Figure 4, and other less stable adsorption configurations and energies are summarized in Figure S5.

As shown in Figure 4, the H atom prefers the C$_A$ (or C$_A$′) sites on pure and metal-doped surfaces. On pure $Mo_2C(101)$, the adsorption energy at the C$_A$ site is −0.46 eV (Figure 4a), much stronger than that at the other adsorption sites (Figure S5). Based on the results on pure $Mo_2C(101)$, we mainly considered the different top sites for H adsorption on the 4M− and 8M−$Mo_2C(101)$ surfaces. On 4M−$Mo_2C(101)$, it is interesting to note that H adsorption has stronger adsorption energy at the top of C$_A$′ site than at the C$_A$ site (−0.64 vs −0.43 eV, −0.69 vs −0.43 eV, −0.70 vs −0.42 eV, −0.67 vs −0.43 eV, −0.59 vs −0.41 eV, and −0.58 vs −0.41 eV for M = Fe, Co, Ni, Cu, Pd, and Pt, respectively), while H does not adsorb at all other sites. On 8M−$Mo_2C(101)$, the adsorption energies at the top of the C$_A$′ site for M = Fe, Co, Ni, Cu, Pd, and Pt are −0.70, −0.88, −0.90, −0.68, −0.75, and −0.73 eV, respectively. These results show that the doping metal promotes hydrogen atom adsorption at the top site of the surface carbon atom. On the contrary, the adsorption of the

https://doi.org/10.1021/acs.jpcc.1c03372
J. Phys. Chem. C 2021, 125, 11419−11431

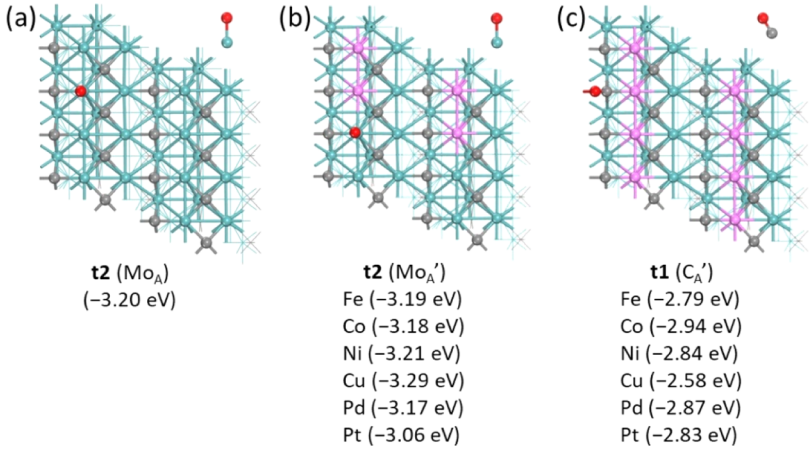

Figure 7. Most stable adsorption configurations and energies (in parentheses) of O on (a) pure $Mo_2C(101)$, (b) 4M−$Mo_2C(101)$, and (c) 8M−$Mo_2C(101)$ (M = Fe, Co, Ni, Cu, Pd, and Pt; O: red, C: gray, Mo: cyan, M: pink; using gaseous O_2 as a reference).

Table 2. Dissociation Barrier (E_a, eV) and Reaction Energy (ΔE_r, eV) as Well as the Critical O−H Distance (d, Å) in the Transition State

	$H_2O \rightarrow TS1 \rightarrow OH + H$			$OH + H \rightarrow TS2 \rightarrow O + 2H$		
surfaces	E_a	ΔE_r	d (TS1)	E_a	ΔE_r	d (TS2)
$Mo_2C(101)$	0.23	−0.94	1.307	0.72	−0.30	1.314
4Fe−$Mo_2C(101)$	0.28	−0.79	1.311	0.77	−0.38	1.325
4Co−$Mo_2C(101)$	0.31	−0.87	1.312	0.80	−0.40	1.316
4Ni−$Mo_2C(101)$	0.30	−0.75	1.306	0.79	−0.39	1.319
4Cu−$Mo_2C(101)$	0.27	−0.90	1.304	0.77	−0.40	1.321
4Pd−$Mo_2C(101)$	0.31	−0.73	1.318	0.81	−0.39	1.325
4Pt−$Mo_2C(101)$	0.36	−0.62	1.326	0.81	−0.37	1.316
8Fe−$Mo_2C(101)$	0.10	−0.48	1.313	0.65	−0.58	1.354
8Co−$Mo_2C(101)$	0.08	−0.72	1.265	0.60	−0.70	1.326
8Ni−$Mo_2C(101)$	0.05	−0.61	1.278	0.68	−0.64	1.360
8Cu−$Mo_2C(101)$	0.05	−0.53	1.307	0.73	−0.49	1.388
8Pd−$Mo_2C(101)$	0.18	−0.40	1.307	0.87	−0.55	1.410
8Pt−$Mo_2C(101)$	0.21	−0.40	1.302	0.85	−0.51	1.388

hydrogen atom around the doping metal has either negligible or endothermic adsorption energies.

H_2O Dissociative Adsorption. Figure 5 shows the most stable H_2O adsorption configurations on all these surfaces, and the less stable adsorption configurations are listed in Figure S6. On pure $Mo_2C(101)$, H_2O prefers the **t2** (Mo_A) site with an adsorption energy of −0.61 eV,[16] while adsorption on the **t4** (Mo_B) site is less stable (−0.31 eV, Figure S6). For 4M−$Mo_2C(101)$, H_2O also prefers the **t2** (Mo_A') site for all doped surfaces with adsorption energies of −0.65, −0.70, −0.68, −0.64, −0.67, and −0.70 eV for M = Fe, Co, Ni, Cu, Pd, and Pt, respectively (Figure 5b), while adsorption at other top sites, **t2** (M), **t4** (Mo_B), and **t4** (Mo_B'), is much less stable. It is also to note that metal doping increases slightly the adsorption energy.

On 8M−$Mo_2C(101)$, H_2O prefers the **t4** (Mo_B') site with adsorption energies of −0.46, −0.50, −0.50, −0.40, −0.37, and −0.41 eV for M = Fe, Co, Ni, Cu, Pd, and Pt, respectively (Figure 5c), while H_2O adsorption at the top of the **t2** (M) doping metal is less stable with adsorption energies of −0.40, −0.38, −0.27, −0.28, −0.15, and −0.10 eV for M = Fe, Co, Ni, Cu, Pd, and Pt, respectively (Figure S6).

Next, we computed the adsorption of OH and O, the intermediates of H_2O dissociative adsorption. For OH, the most stable adsorption configurations are shown in Figure 6, and the other less stable adsorption configurations are listed in Figure S7.

On pure $Mo_2C(101)$ (Figure 6a), OH prefers the **b1** (Mo_A−Mo_A) site with an adsorption energy of −4.26 eV, followed by that at the **t2** (Mo_A) site (−3.85 eV), while adsorption at other sites (**t4**, **b4**, **b3**, and **t3**) is much less stable. On 4M−$Mo_2C(101)$, OH also prefers the **b1** (Mo_A'−Mo_A') site with adsorption energies of −4.18, −4.13, −4.18, −4.27, −4.14, and −4.06 eV for M = Fe, Co, Ni, Cu, Pd, and Pt, respectively (Figure 6b). Since OH prefers the bridge sites over the top sites, we also computed other bridge sites, **b1** (M−Mo_A') and **b1** (M−M) as well as **b3** (Mo_B−Mo_B), **b3** (Mo_B'−Mo_B), and **b3** (Mo_B'−Mo_B'), and all these sites have lower OH adsorption energies (Figure S7).

On 8M−$Mo_2C(101)$, dramatic changes have been found. For M = Co and Pt (Figure 6c,d), **b5** (C_A'−Mo_B') and **b3** (Mo_B'−Mo_B') sites have the same adsorption energy (−3.62 and −3.46 eV, respectively). For M = Ni and Pd, the **b5** (C_A'−Mo_B') site has a stronger adsorption energy than the **b3** (Mo_B'−Mo_B') site (−3.60 vs −3.42 eV for Ni and −3.46 vs −3.39 eV for Pd). For M = Fe and Cu, the **b3** (Mo_B'−Mo_B') and **b5** (C_A'−Mo_B') sites have close adsorption energies (−3.48 vs −3.46 eV for Fe and −3.41 vs −3.37 eV for Cu). On the contrary, the **b1** (M−M) site has much lower OH adsorption energy (Figure S7). It shows that metal doping can

https://doi.org/10.1021/acs.jpcc.1c03372
J. Phys. Chem. C 2021, 125, 11419−11431

Scheme 1. Potential Energy Surface of H_2O Dissociative Adsorption on (a) 4M−Mo_2C(101), Left, and (b) 8M−Mo_2C(101), Right (M = Mo, Fe, Co, Ni, Cu, Pd, and Pt; the Magnified Surface in the Dash Line Square)

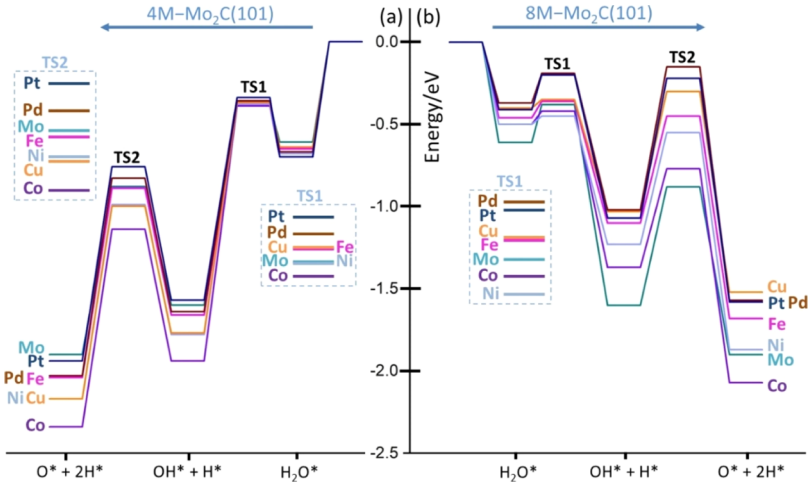

lower OH adsorption energy to a large extent on the 8M−Mo_2C(101) surfaces by about 15−20%, and this might affect the reactions associated with surface OH.

Next, we computed surface oxygen adsorption (Figure 7). On pure Mo_2C(101), O prefers the **t2** (Mo_A) site with an adsorption energy of −3.20 eV. Similarly, O also prefers the **t2** (Mo_A') site on 4M−Mo_2C(101) with adsorption energies close to that on the pure surface. On 8M−Mo_2C(101), however, O prefers the **t1** (C_A') site with adsorption energies of −2.79, −2.94, −2.84, −2.58, −2.87, and −2.83 eV for M = Fe, Co, Ni, Cu, Pd, and Pt, respectively. The **t4** (Mo_B') site is the second most stable site with adsorption energies of −2.44, −2.49, −2.54,−2.35, −2.52, and −2.53 eV for M = Fe, Co, Ni, Cu, Pd, and Pt, respectively. It is also noted that O adsorption at the **t2** (M) site has a very low or even positive adsorption energy and therefore not favored. It shows that metal doping can lower the adsorption energy to a large extent on the 8M−Mo_2C(101) surfaces by about 10−20%, and this might affect the reactions associated with surface O.

On the basis of these most stable adsorption sites of H_2O, OH, O, and H, we explored H_2O sequential dissociation on these surfaces. The barriers, reation energies, and breaking bond distances are listed in Table 2, and the adsorption structures of the IS, TS, and FS are summarized in Figures S9 and S10. The simplified potential energy surfaces are shown in Scheme 1.

On the pure Mo_2C(101) and 4M−Mo_2C(101) surfaces, the adsorption configurations of the first H_2O dissociation step ($H_2O \rightarrow OH + H$) are very similar since they start at the Mo_A or Mo_A' sites, and the potential energy surfaces are also very similar (Scheme 1a, left). Compared to the pure Mo_2C(101) surface (0.23 and −0.94 eV), the dissociation barrier becomes higher, while the dissociation energy becomes less exothermic, and the largest change has been found for Pt doping (0.36 and −0.62 eV). In addition, the corresponding transition states also have similar breaking O−H distances (Table 2).

For the second dissociation step ($OH + H \rightarrow O + 2H$), their configurations in IS, TS, and FS are also similar on both pure and 4 M−Mo_2C(101) surfaces (Figure S10) but vary in H atom migration. After the first dissociation step, the H atom migrates to the more stable remote site (C_A or C_A') which is also the most stable adsorption site for the pure single H atom (Figure 4). Compared to the pure Mo_2C(101) surface (0.72 and −0.30 eV), the dissociation barrier increases slightly (0.81 eV for Pd and Pt) and the dissociation energy becomes slightly more exothermic (−0.40 eV for Cu and Co). In addition, the corresponding transition states have similar breaking O−H distances (Table 2).

On the 8M−Mo_2C(101) surface, where all Mo_A atoms are replaced with doping metal atoms, H_2O adsorbs at the **t4** (Mo_B') sites (Figure S9). The adsorption configuration of the first H_2O dissociation step ($H_2O \rightarrow OH + H$) is similar compared to pure and 4M−Mo_2C(101) but with different orientation for O−H bond breaking. As shown in Scheme 1b (right), H_2O has not only lower adsorption energy but also a much lower barrier for the first-step H_2O dissociation ($H_2O \rightarrow OH + H$), as compared to the 4M−Mo_2C(101) and pure Mo_2C surfaces. In addition, the first dissociation step on 8M−Mo_2C(101) is also much less exothermic than that on the 4M−Mo_2C(101) and pure Mo_2C surfaces. Compared to the 4M−Mo_2C(101) surface, the barrier of the second dissociation step ($OH + H \rightarrow O + 2H$) is lower for M = Fe, Co, Ni, and Cu but higher for M = Pd and Pt, while the reaction is more exothermic.

In addition to the individual steps, the general trend of H_2O dissociative adsorption over 4M- and 8M-doped surfaces in comparison with the pure surface can be seen in Scheme 1. Due to the similar or same adsorption site of the 4M-doped surface (Mo_A' vs Mo_A) and the pure surface (Scheme 1, left), the same trend has been found, that is, the first H_2O dissociation step has a barrier lower than the H_2O adsorption energy and the dissociation is very exothermic, indicating that dissociation is more preferred than desorption. Next, the second dissociation step has a higher barrier and is less exothermic than the first dissociation step. Compared to the pure surface, the total reaction on the 4M-doped surface is more exothermic, indicating the enhanced thermodynamic trend. This shows that the 4M-doped surface can bind surface intermediates more strongly than the pure surface. On the 8M-doped surface with Mo_B' as the favored adsorption site, the first H_2O dissociation step also has a barrier lower than the H_2O adsorption energy, and the dissociation is very exothermic, indicating that dissociation is more preferred than desorption, and the dissociation is less exothermic than that on the pure surface. All these changes are to a lesser extent than those on the corresponding 4M-doped surfaces. Different

https://doi.org/10.1021/acs.jpcc.1c03372
J. Phys. Chem. C 2021, 125, 11419−11431

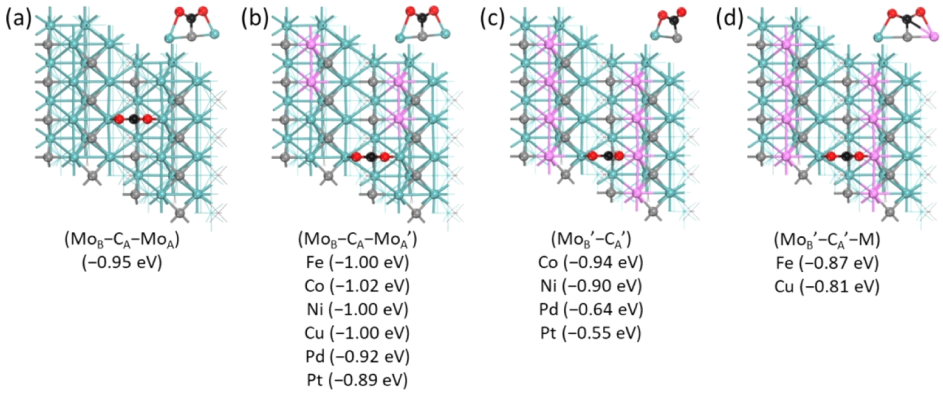

Figure 8. Most stable adsorption configurations and energies (in parentheses) of CO_2 on (a) pure $Mo_2C(101)$, (b) 4M−$Mo_2C(101)$, and (c,d) 8M−$Mo_2C(101)$ (M = Fe, Co, Ni, Cu, Pd, and Pt; O: red, C in CO_2: black, C in Mo_2C: gray, Mo: cyan, M: pink).

from the 4M-doped surface, the transition state of the second dissociation step is higher in energy for M = Cu and Pd and lower in energy for M = Fe, Co, Ni, and Pt than that of the first dissociation step, indicating that surface OH can be a stable intermediate for M = Cu and Pd. Next, the second dissociation step has a higher barrier than the first dissociation step, and the reaction energy is close to the first dissociation step. Compared to the pure surface, the total reaction on the 8M-doped surface is less exothermic apart from M = Co, indicating the doping metal dependence.

CO_2 Dissociative Adsorption. The adsorption of CO_2 on the pure and metal doping surfaces is computed, and the most stable adsorption configurations are listed in Figure 8, while the less stable configurations and energies are listed in Figure S11.

On pure $Mo_2C(101)$, the most stable adsorption configuration of CO_2 has a tridentate mode, in which the C atom interacts with surface C_A and the O atoms interact with surface Mo_A and Mo_B, and the adsorption energy is −0.95 eV, followed by that at the **b1** (Mo_A−Mo_A) site (Figure S11, −0.90 eV), and the **b3** (Mo_B−Mo_B) site has a positive adsorption energy (Figure S11, 0.45 eV). On the 4M−$Mo_2C(101)$ surface (Figure 8b), the most stable CO_2 adsorption has the same configuration and similar energy as on the pure surface, while CO_2 adsorption at the Mo_B−C_A'−M site is less stable (Figure S11). In addition, CO_2 adsorption at other bridge sites also becomes less stable or has a positive adsorption energy. On 8M−$Mo_2C(101)$, the most stable CO_2 adsorption has a bidentate mode for M = Co, Ni, Pd, and Pt, in which the C atom interacts with surface C_A' and one O atom interacts with Mo_B' and another O atom does not interact with the doping atom, and a tridentate mode for M = Fe and Cu; also, the adsorption energies are lower than those on 4M−$Mo_2C(101)$. Besides, their corresponding C−O stretching frequencies are also calculated (Table S2). The stretching frequencies are similar between the 4M−$Mo_2C(101)$ and pure $Mo_2C(101)$ surfaces due to their similar adsorption configurations. On the 8M−$Mo_2C(101)$ surfaces, significant differences in C−O stretching frequencies between the bidentate modes (Fe and Cu) compared to tridentate (Co, Ni, Pd, and Pt) adsorption configurations are found.

On the basis of the most stable adsorption configurations of CO_2, CO (Figure 2), and O (Figure 7), we computed CO_2 dissociation on these surfaces. The barriers, reation energies, and breaking C−O bond distances are listed in Table 3, and the adsorption structures of the IS, TS, and FS are given in Figure S12. The simplified potential energy surfaces are shown in Scheme 2.

Table 3. Dissociation Barrier (E_a, eV), Reaction Energy (ΔE_r, eV), and Critical C−O Distance (d, Å) in the Transition State

surfaces	$CO_2 \rightarrow TS \rightarrow CO + O$		
	E_a	ΔE_r	d (TS)
$Mo_2C(101)$	0.56	−0.63	1.602
4Fe−$Mo_2C(101)$	0.31	−0.70	1.640
4Co−$Mo_2C(101)$	0.48	−0.68	1.648
4Ni−$Mo_2C(101)$	0.16	−0.76	1.660
4Cu−$Mo_2C(101)$	0.05	−0.86	1.665
4Pd−$Mo_2C(101)$	0.16	−0.76	1.661
4Pt−$Mo_2C(101)$	0.28	−0.66	1.660
8Fe−$Mo_2C(101)$	0.97	0.30	1.917
8Co−$Mo_2C(101)$	0.50	0.09	1.620
8Ni−$Mo_2C(101)$	0.80	0.33	1.717
8Cu−$Mo_2C(101)$	0.82	0.56	1.652
8Pd−$Mo_2C(101)$	0.88	0.57	1.700
8Pt−$Mo_2C(101)$	0.83	0.50	1.694

On the pure surface, CO_2 dissociation has a barrier (0.56 eV) lower than the adsorption energy (−0.95 eV) and is exothermic (−0.63 eV), and the same trend is found on 4M−$Mo_2C(101)$ with a lower barrier and the dissociation is more exothermic, indicating that the doping metal can promote CO_2 dissociation, although it does not participate in CO_2 dissociation directly. On 8M−$Mo_2C(101)$, totally different results have been found, that is, CO_2 dissociation becomes endothermic compared to that on the pure and 4M-doped surfaces, indicating the doping effect. In addition to these individual values, the general trend can be seen in Scheme 2. It shows that on pure and 4M-doped surfaces, CO_2 dissociation barriers are lower than their adsorption energy, indicating that dissociation is favored over desorption. In addition, the dissociated state is in close energy to that on the pure surface for M = Fe, Co, Ni, and Pd but less stable for M = Pt and more stable for M = Cu. On 8M−$Mo_2C(101)$, the CO_2 dissociation barrier is higher than the adsorption energy for M = Fe, Pd, and Pt, close to that of Cu, and lower than that for M = Ni and Co. This indicates that at an elevated temperature, CO_2 desorption is more preferred than dissociation for M = Fe, Pd, and Pt, while molecular and dissociative adsorption might have equilibrium for M = Ni, Cu, and Co.

https://doi.org/10.1021/acs.jpcc.1c03372
J. Phys. Chem. C 2021, 125, 11419−11431

Scheme 2. Potential Energy Surface of CO_2 Dissociative Adsorption on (a) 4M−Mo_2C(101), Left, and (b) 8M−Mo_2C(101), Right (M = Mo, Fe, Co, Ni, Cu, Pd, and Pt; the Magnified Surface in the Dash Line Square)

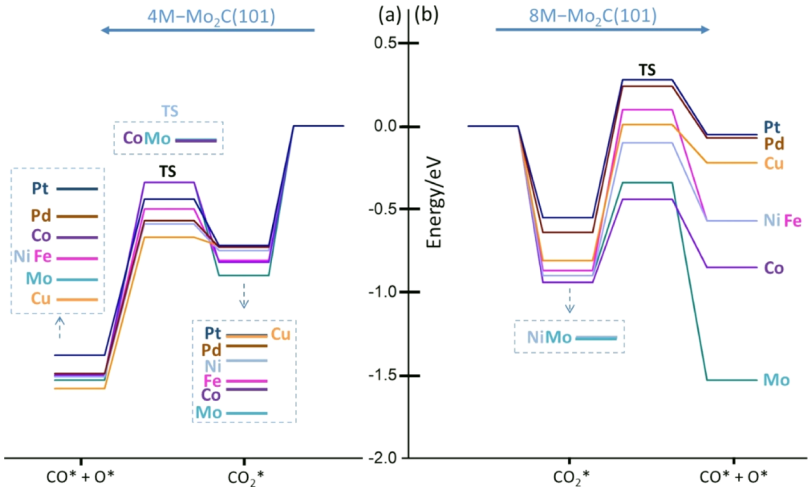

Scheme 3. Comparative Adsorption Energies of CO, OH, O, and H on Mo_2C(101), 4M−Mo_2C(101), and 8M−Mo_2C(101) and the Corresponding Metallic Low-Index Surfaces (M = Fe, Co, Ni, Cu, Pd, and Pt)

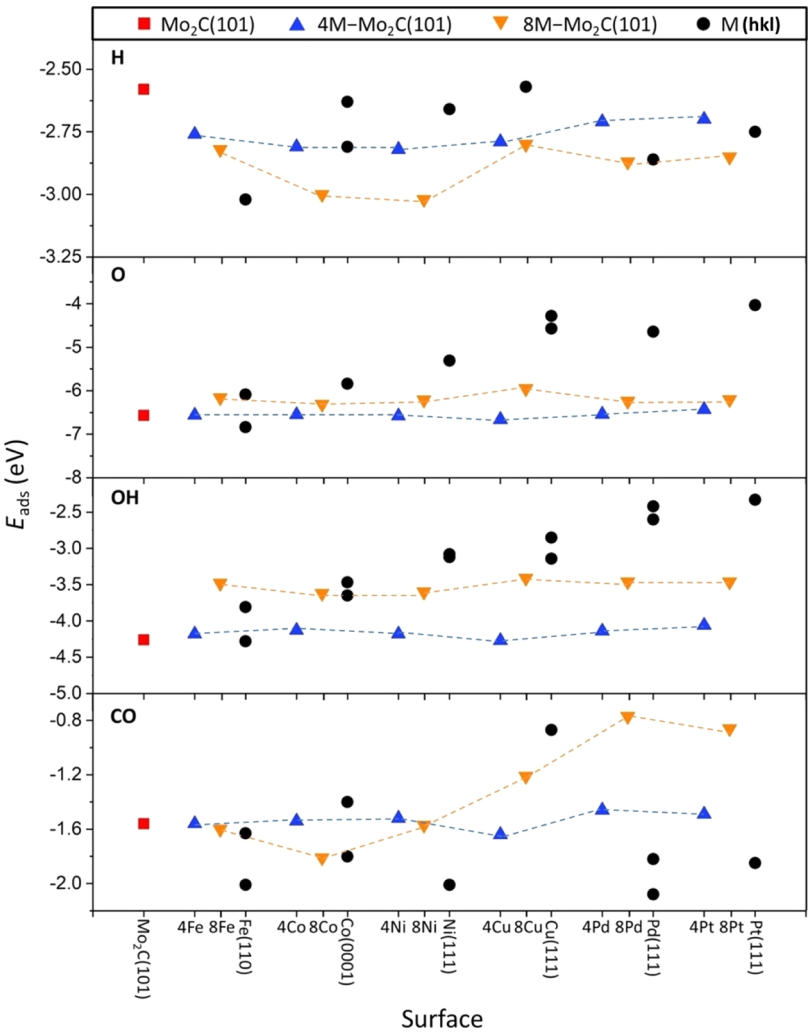

Since both metals and supports play decisive and unique roles in heterogeneous catalysis, we compared the adsorption properties of surface CO, OH, O, and H species, which are intermediates of many catalytic reactions, on the pure and metal-doped Mo_2C(101) surfaces as well as on the corresponding metallic low-index Fe(110),[43−47] Co(0001),[43,48−50] Ni(111),[43,51−54] Cu(111),[43,54−56] Pd(111),[43,54,57,58] and Pt(111)[43,54,59−61] surfaces. For making

https://doi.org/10.1021/acs.jpcc.1c03372
J. Phys. Chem. C 2021, 125, 11419−11431

as close comparison as possible, we compiled all these reported data using the same or nearly the same methodology despite their different adsorption sites and configurations (Table S3); and the general trend is shown in Scheme 3.

For CO adsorption, the adsorption energy on the pure and 4M-doped $Mo_2C(101)$ surfaces varies only slightly but strongly on the 8M-doped $Mo_2C(101)$ surfaces. The CO adsorption energies on these surfaces are lower than that of the metallic low-index surfaces apart from Cu(111), which has lower adsorption than the pure M-doped $Mo_2C(101)$ surfaces. For the adsorption of surface OH and O species, the adsorption energies on the pure and 4M-doped $Mo_2C(101)$ surfaces are more or less the same but stronger than those on the 8M-doped $Mo_2C(101)$ surfaces, and all these adsorption energies are stronger than those on the metallic low-index surfaces. For the adsorption of atomic hydrogen, the adsorption energies on the 4M- and 8M-doped surfaces are stronger than that on the pure surface, and the 8M-doped surfaces have stronger adsorption energies than the 4M-doped surface apart from 4Cu- and 8Cu-doped surfaces which have nearly the same adsorption energies. Compared to the pure and M-doped $Mo_2C(101)$ surfaces, Fe(110) has stronger adsorption energy, while Co(0001), Ni(111), and Cu(111) have weaker adsorption energies. Pd(111)- and 8Pd-doped surfaces have similar adsorption energies, and Pt(111) has adsorption energy between 4Pt- and 8Pt-doped surfaces. All these show their similarity and differences in adsorption, which should also be reflected in their catalytic kinetics and thermodynamics.

■ CONCLUSIONS

Experimentally, supported transition-metal catalysts in heterogeneous catalysis show different activity from only metals and pure supports due to their enhanced mutual and synergistic interaction. To understand these effects, we computed transition-metal doping on the hexagonal $Mo_2C(101)$ surface by substituting the less coordinated and more active surface Mo_A atoms with Fe, Co, Ni, Cu, Pd, and Pt in 4M (25%) and 8M (50%) metal loading.

It is found that metal doping affects the surface electronic properties based on the analysis of PDOS and creates more adsorption sites by changing the coordination environment for surface metal and carbons atoms. Strong electron transfer from the metal to the surface has been found for Fe, Co, Ni, and Cu, resulting in a positive Bader charge on the doping metal, and this agrees with the experimentally observed effect for Cu-doped Mo_2C. On the contrary, much less electron transfer from Pd to the surface or from the surface to Pt has been found. Consequently, not only surface metal atoms but also surface carbon atoms become active in adsorption of surface species.

On the pure and 4M (25%)-doped surfaces, surface Mo_A atoms are most preferred sites for the adsorption of H_2, H_2O, OH, and O, and surface carbon (C_A) atoms are responsible for the adsorption of H atoms, while surface Mo_A and C_A are co-responsible for the adsorption of CO and CO_2. On the 8M (50%)-doped surfaces, the less active surface Mo_B and surface C_B become active for the adsorption of CO and CO_2, and the adsorption energy depends on the doping metals. It is also found that molecular H_2 has physisorption preferring the top of the doping metal, while atomic H prefers the top of the surface C_A atom forming the C−H bond. The adsorption of H_2O and OH prefers the top and bridge sites, respectively, while atomic O prefers the top site of the surface C_A atom forming the C−O bond. Depending on doping metals and adsorption sites, the adsorption of each surface species can become more or less exothermic compared to the pure surface.

On the basis of these results, we explored the dissociative adsorption of H_2O and CO_2 and found potential energy surfaces depending on the metal and loading. Full H_2O dissociative adsorption is favored thermodynamically on the 4M-doped surfaces and more exothermic compared to that on the pure surface but less exothermic and doping-metal-dependent on the 8M-doped surfaces apart from Co. CO_2 dissociative adsorption is thermodynamically favored on the 4M-doped surfaces but becomes endothermic on the 8M-doped surface, preferring molecular instead of dissociative adsorption for Co, Ni, Cu, Pd, and Pt as well as equilibrium between molecular and dissociative adsorption for Co. Comparing the adsorption of CO, OH, O, and H on the pure and doped $Mo_2C(101)$ surfaces and the corresponding metallic M(*hkl*) surfaces reveals their similarity and difference, and these should also be found in the reaction kinetics and thermodynamics. These results provide a basis for studying the mechanisms of reactions involving these surface species, for example, the reported promotion effect in water-gas reaction, methanol reforming, and evolution reaction of hydrogen and oxygen.

■ ASSOCIATED CONTENT

Supporting Information

The Supporting Information is available free of charge at https://pubs.acs.org/doi/10.1021/acs.jpcc.1c03372.

PDOS; adsorption configurations and energies; energy barriers and structural parameters of IS, TS, and FS involved in H_2O and CO_2 dissociation; stretching frequency of CO; and bond distance (PDF)

■ AUTHOR INFORMATION

Corresponding Author

Haijun Jiao − *Leibniz-Institut für Katalyse e.V. an der Universität Rostock, Rostock 18059, Germany;* orcid.org/0000-0002-2947-5937; Email: haiju.jiao@catalysis.de

Authors

Fan Wang − *Leibniz-Institut für Katalyse e.V. an der Universität Rostock, Rostock 18059, Germany*

Xinxin Tian − *Leibniz-Institut für Katalyse e.V. an der Universität Rostock, Rostock 18059, Germany; Institute of Molecular Science, Key Laboratory of Materials for Energy Conversion and Storage of Shanxi Province, Shanxi University, Taiyuan 030006, China*

Complete contact information is available at: https://pubs.acs.org/10.1021/acs.jpcc.1c03372

Notes

The authors declare no competing financial interest.

■ ACKNOWLEDGMENTS

F.W. thanks the support of the China Scholarship Council (CSC), and X.T. thanks the financial support from the National Natural Science Foundation of China (no. 21903049). The general financial support from the BMBF and the state of Mecklenburg−Vorpommern, Germany, is acknowledged.

REFERENCES

(1) Valden, M.; Lai, X.; Goodman, D. W. Onset of Catalytic Activity of Gold Clusters on Titania with the Appearance of Nonmetallic Properties. *science* **1998**, *281*, 1647−1650.

(2) Navlani-García, M.; Salinas-Torres, D.; Mori, K.; Kuwahara, Y.; Yamashita, H. Tailoring the Size and Shape of Colloidal Noble Metal Nanocrystals as a Valuable Tool in Catalysis. *Catal. Surv. Asia* **2019**, *23*, 127−148.

(3) Ruditskiy, A.; Peng, H.-C.; Xia, Y. Shape-Controlled Metal Nanocrystals for Heterogeneous Catalysis. *Annu. Rev. Chem. Biomol. Eng.* **2016**, *7*, 327−348.

(4) Lane, M. K. M.; Zimmerman, J. B. Controlling Metal Oxide Nanoparticle Size and Shape with Supercritical Fluid Synthesis. *Green Chem.* **2019**, *21*, 3769−3781.

(5) Cao, A.; Lu, R.; Veser, G. Stabilizing Metal Nanoparticles for Heterogeneous Catalysis. *Phys. Chem. Chem. Phys.* **2010**, *12*, 13499−13510.

(6) De Rogatis, L.; Cargnello, M.; Gombac, V.; Lorenzut, B.; Montini, T.; Fornasiero, P. Embedded Phases: A Way to Active and Stable Catalysts. *ChemSusChem* **2010**, *3*, 24−42.

(7) dos Santos Politi, J. R.; Viñes, F.; Rodriguez, J. A.; Illas, F. Atomic and Electronic Structure of Molybdenum Carbide Phases: Bulk and Low Miller-Index Surfaces. *Phys. Chem. Chem. Phys.* **2013**, *15*, 12617−12625.

(8) Széchenyi, A.; Solymosi, F. Production of Hydrogen in the Decomposition of Ethanol and Methanol over Unsupported Mo_2C Catalysts. *J. Phys. Chem. C* **2007**, *111*, 9509−9515.

(9) Barthos, R.; Széchenyi, A.; Solymosi, F. Efficient H_2 Production from Ethanol over Mo_2C/C Nanotube Catalyst. *Catal. Lett.* **2008**, *120*, 161−165.

(10) Ma, Y.; Guan, G.; Shi, C.; Zhu, A.; Hao, X.; Wang, Z.; Kusakabe, K.; Abudula, A. Low-Temperature Steam Reforming of Methanol to Produce Hydrogen over Various Metal-Doped Molybdenum Carbide Catalysts. *Int. J. Hydrogen Energy* **2014**, *39*, 258−266.

(11) Ma, Y.; Guan, G.; Hao, X.; Zuo, Z.; Huang, W.; Phanthong, P.; Kusakabe, K.; Abudula, A. Highly-Efficient Steam Reforming of Methanol over Copper Modified Molybdenum Carbide. *RSC Adv.* **2014**, *4*, 44175−44184.

(12) Ma, Y.; Guan, G.; Hao, X.; Zuo, Z.; Huang, W.; Phanthong, P.; Li, X.; Kusakabe, K.; Abudula, A. Embedded Structure Catalyst: A New Perspective from Noble Metal Supported on Molybdenum Carbide. *RSC Adv.* **2015**, *5*, 15002−15005.

(13) Wan, C.; Leonard, B. M. Iron-Doped Molybdenum Carbide Catalyst with High Activity and Stability for the Hydrogen Evolution Reaction. *Chem. Mater.* **2015**, *27*, 4281−4288.

(14) Liu, Y.; Ding, J.; Bi, J.; Sun, Y.; Zhang, J.; Liu, K.; Kong, F.; Xiao, H.; Chen, J. Effect of Cu-Doping on the Structure and Performance of Molybdenum Carbide Catalyst for Low-Temperature Hydrogenation of Dimethyl Oxalate to Ethanol. *Appl. Catal., A* **2017**, *529*, 143−155.

(15) Liu, P.; Rodriguez, J. A. Water-Gas-Shift Reaction on Molybdenum Carbide Surfaces: Essential Role of the Oxycarbide. *J. Phys. Chem. B* **2006**, *110*, 19418−19425.

(16) Shi, Y.; Yang, Y.; Li, Y.-W.; Jiao, H. Activation Mechanisms of H_2, O_2, H_2O, CO_2, CO, CH_4 and C_2H_X on Metallic $Mo_2C(001)$ as Well as Mo/C Terminated $Mo_2C(101)$ from Density Functional Theory Computations. *Appl. Catal., A* **2016**, *524*, 223−236.

(17) Wang, F.; Li, T.; Jiao, H. Nitridation of the Metallic Mo_2C (001) Surface from NH_3 Dissociative Adsorption—a Dft Study. *Surf. Sci.* **2019**, *689*, 121466.

(18) Krasheninnikov, A. V.; Lehtinen, P. O.; Foster, A. S.; Pyykkö, P.; Nieminen, R. M. Embedding Transition-Metal Atoms in Graphene: Structure, Bonding, and Magnetism. *Phys. Rev. Lett.* **2009**, *102*, 126807.

(19) Zhou, M.; Cheng, L.; Choi, J.-S.; Liu, B.; Curtiss, L. A.; Assary, R. S. Ni-Doping Effects on Oxygen Removal from an Orthorhombic Mo_2C (001) Surface: A Density Functional Theory Study. *J. Phys. Chem. C* **2018**, *122*, 1595−1603.

(20) Chen, Y.-Y.; Dong, M.; Wang, J.; Jiao, H. Mechanisms and Energies of Water Gas Shift Reaction on Fe-, Co-, and Ni-Promoted MoS_2 Catalysts. *J. Phys. Chem. C* **2012**, *116*, 25368−25375.

(21) Wang, T.; Liu, X.; Wang, S.; Huo, C.; Li, Y.-W.; Wang, J.; Jiao, H. Stability of β-Mo_2C Facets from Ab Initio Atomistic Thermodynamics. *J. Phys. Chem. C* **2011**, *115*, 22360−22368.

(22) Haines, J.; Léger, J. M.; Chateau, C.; Lowther, J. E. Experimental and Theoretical Investigation of Mo_2C at High Pressure. *J. Phys.: Condens. Matter* **2001**, *13*, 2447−2454.

(23) Wang, X.-H.; Hao, H.-L.; Zhang, M.-H.; Li, W.; Tao, K.-Y. Synthesis and Characterization of Molybdenum Carbides Using Propane as Carbon Source. *J. Solid State Chem.* **2006**, *179*, 538−543.

(24) Kresse, G.; Furthmüller, J. Efficiency of Ab-Initio Total Energy Calculations for Metals and Semiconductors Using a Plane-Wave Basis Set. *Comput. Mater. Sci.* **1996**, *6*, 15−50.

(25) Kresse, G.; Furthmüller, J. Efficient Iterative Schemes for Ab Initio Total-Energy Calculations Using a Plane-Wave Basis Set. *Phys. Rev. B: Condens. Matter Mater. Phys.* **1996**, *54*, 11169−11186.

(26) Blöchl, P. E. Projector Augmented-Wave Method. *Phys. Rev. B: Condens. Matter Mater. Phys.* **1994**, *50*, 17953−17979.

(27) Perdew, J. P.; Burke, K.; Ernzerhof, M. Generalized Gradient Approximation Made Simple. *Phys. Rev. Lett.* **1996**, *77*, 3865−3868.

(28) Henkelman, G.; Uberuaga, B. P.; Jónsson, H. A Climbing Image Nudged Elastic Band Method for Finding Saddle Points and Minimum Energy Paths. *J. Chem. Phys.* **2000**, *113*, 9901−9904.

(29) Wang, T.; Li, Y.-W.; Wang, J.; Beller, M.; Jiao, H. Dissociative Hydrogen Adsorption on the Hexagonal Mo_2C Phase at High Coverage. *J. Phys. Chem. C* **2014**, *118*, 8079−8089.

(30) CHRISTENSEN, A. N.; Kvande, H.; Wahlbeck, P. G.; Näsäkkälä, E. A Neutron Diffraction Investigation on a Crystal of alpha-Mo_2C. *Acta Chem. Scand., Ser. A* **1977**, *31*, 509−511.

(31) Dubois, J.; Epicier, T.; Esnouf, C.; Fantozzi, G.; Convert, P. Neutron Powder Diffraction Studies of Transition Metal Hemicarbides M_2C_{1-X}—I. Motivation for a Study on W_2C and Mo_2C and Experimental Background for an in Situ Investigation at Elevated Temperature. *Acta Metall.* **1988**, *36*, 1891−1901.

(32) Epicier, T.; Dubois, J.; Esnouf, C.; Fantozzi, G.; Convert, P. Neutron Powder Diffraction Studies of Transition Metal Hemicarbides M_2C_{1-X}—II. In Situ High Temperature Study on W_2C_{1-X} and Mo_2C_{1-X}. *Acta Metall.* **1988**, *36*, 1903−1921.

(33) Shi, Y.; Yang, Y.; Li, Y.-W.; Jiao, H. Theoretical Study About $Mo_2C(101)$-Catalyzed Hydrodeoxygenation of Butyric Acid to Butane for Biomass Conversion. *Catal. Sci. Technol.* **2016**, *6*, 4923−4936.

(34) Fries, R. J.; Kempter, C. P. 195. Dimolybdenum Carbide. *Anal. Chem.* **1960**, *32*, 1898.

(35) Miyao, T.; Shishikura, I.; Matsuoka, M.; Nagai, M.; Oyama, S. T. Preparation and Characterization of Alumina-Supported Molybdenum Carbide. *Appl. Catal., A* **1997**, *165*, 419−428.

(36) Wang, T.; Li, Y.-W.; Wang, J.; Beller, M.; Jiao, H. High Coverage Co Adsorption and Dissociation on the Orthorhombic $Mo_2C(100)$ Surface. *J. Phys. Chem. C* **2014**, *118*, 3162−3171.

(37) Wang, T.; Wang, S.; Li, Y.-W.; Wang, J.; Jiao, H. Adsorption Equilibria of Co Coverage on β-Mo_2C Surfaces. *J. Phys. Chem. C* **2012**, *116*, 6340−6348.

(38) Wang, T.; Tian, X.; Yang, Y.; Li, Y.-W.; Wang, J.; Beller, M.; Jiao, H. Coverage Dependent Adsorption and Co-Adsorption of Co and H_2 on the CdI_2-Antitype Metallic $Mo_2C(001)$ Surface. *Phys. Chem. Chem. Phys.* **2015**, *17*, 1907−1917.

(39) Grimme, S. Semiempirical Gga-Type Density Functional Constructed with a Long-Range Dispersion Correction. *J. Comput. Chem.* **2006**, *27*, 1787−1799.

(40) Hugosson, H. W.; Eriksson, O.; Jansson, U.; Johansson, B. Phase Stabilities and Homogeneity Ranges in 4d-Transition-Metal Carbides: A Theoretical Study. *Phys. Rev. B: Condens. Matter Mater. Phys.* **2001**, *63*, 134108.

(41) Henkelman, G.; Arnaldsson, A.; Jónsson, H. A Fast and Robust Algorithm for Bader Decomposition of Charge Density. *Comput. Mater. Sci.* **2006**, *36*, 354−360.

https://doi.org/10.1021/acs.jpcc.1c03372
J. Phys. Chem. C 2021, 125, 11419−11431

(42) Allen, L. C. Electronegativity Is the Average One-Electron Energy of the Valence-Shell Electrons in Ground-State Free Atoms. *J. Am. Chem. Soc.* **1989**, *111*, 9003−9014.
(43) Abild-Pedersen, F.; Andersson, M. P. Co Adsorption Energies on Metals with Correction for High Coordination Adsorption Sites−a Density Functional Study. *Surf. Sci.* **2007**, *601*, 1747−1753.
(44) Xu, L.; Kirvassilis, D.; Bai, Y.; Mavrikakis, M. Atomic and Molecular Adsorption on Fe(110). *Surf. Sci.* **2018**, *667*, 54−65.
(45) Liu, S.; Li, Y.-W.; Wang, J.; Jiao, H. Reactions of CO, H_2O, CO_2, and H_2 on the Clean and Precovered Fe(110) Surfaces−a Dft Investigation. *J. Phys. Chem. C* **2015**, *119*, 28377−28388.
(46) Chakrabarty, A.; Bouhali, O.; Mousseau, N.; Becquart, C. S.; El-Mellouhi, F. Insights on Finite Size Effects in Ab Initio Study of Co Adsorption and Dissociation on Fe 110 Surface. *J. Appl. Phys.* **2016**, *120*, 055301.
(47) Liu, S.; Tian, X.; Wang, T.; Wen, X.; Li, Y.-W.; Wang, J.; Jiao, H. Coverage Dependent Water Dissociative Adsorption on Fe(110) from Dft Computation. *Phys. Chem. Chem. Phys.* **2015**, *17*, 8811−8821.
(48) Luo, W.; Asthagiri, A. Density Functional Theory Study of Methanol Steam Reforming on Co(0001) and Co(111) Surfaces. *J. Phys. Chem. C* **2014**, *118*, 15274−15285.
(49) Ma, Y.; Hernández, L.; Guadarrama-Pérez, C.; Balbuena, P. B. Ethanol Reforming on Co(0001) Surfaces: A Density Functional Theory Study. *J. Phys. Chem. A* **2012**, *116*, 1409−1416.
(50) Gunasooriya, G. T. K. K.; van Bavel, A. P.; Kuipers, H. P. C. E.; Saeys, M. Co Adsorption on Cobalt: Prediction of Stable Surface Phases. *Surf. Sci.* **2015**, *642*, L6−L10.
(51) Eichler, A. Co Adsorption on Ni(111)−−a Density Functional Theory Study. *Surf. Sci.* **2003**, *526*, 332−340.
(52) Zhu, L.; Liu, C.; Wen, X.; Li, Y.-W.; Jiao, H. Coverage-Dependent Water Dissociative Adsorption Properties on Nickel Surfaces. *J. Phys. Chem. C* **2020**, *124*, 25835−25845.
(53) Mohsenzadeh, A.; Bolton, K.; Richards, T. Dft Study of the Adsorption and Dissociation of Water on Ni(111), Ni(110) and Ni(100) Surfaces. *Surf. Sci.* **2014**, *627*, 1−10.
(54) Phatak, A. A.; Delgass, W. N.; Ribeiro, F. H.; Schneider, W. F. Density Functional Theory Comparison of Water Dissociation Steps on Cu, Au, Ni, Pd, and Pt. *J. Phys. Chem. C* **2009**, *113*, 7269−7276.
(55) Wang, J.; Wang, G.-C. Promotion Effect of Methane Activation on Cu(111) by the Surface-Active Oxygen Species: A Combination of Dft and Reaxff Study. *J. Phys. Chem. C* **2018**, *122*, 17338−17346.
(56) Jiang, Z.; Fang, T. Dissociation Mechanism of H_2O on Clean and Oxygen-Covered Cu(111) Surfaces: A Theoretical Study. *Vacuum* **2016**, *128*, 252−258.
(57) Martin, N. M.; Van den Bossche, M.; Grönbeck, H.; Hakanoglu, C.; Zhang, F.; Li, T.; Gustafson, J.; Weaver, J. F.; Lundgren, E. Co Adsorption on Clean and Oxidized Pd(111). *J. Phys. Chem. C* **2014**, *118*, 1118−1128.
(58) Tian, P.; Ouyang, L.; Xu, X.; Xu, J.; Han, Y.-F. Density Functional Theory Study of Direct Synthesis of H_2O_2 from H_2 and O_2 on Pd(111), Pd(100), and Pd(110) Surfaces. *Chin. J. Catal.* **2013**, *34*, 1002−1012.
(59) Lakshmikanth, K. G.; Kundappaden, I.; Chatanathodi, R. A Dft Study of Co Adsorption on Pt(111) Using Van Der Waals Functionals. *Surf. Sci.* **2019**, *681*, 143−148.
(60) Jinnouchi, R.; Kodama, K.; Morimoto, Y. Dft Calculations on H, Oh and O Adsorbate Formations on Pt(111) and Pt(332) Electrodes. *J. Electroanal. Chem.* **2014**, *716*, 31−44.
(61) Offermans, W. K.; Jansen, A. P. J.; van Santen, R. A.; Novell-Leruth, G.; Ricart, J. M.; Pérez-Ramírez, J. Ammonia Dissociation on Pt{100}, Pt{111}, and Pt{211}: A Comparative Density Functional Theory Study. *J. Phys. Chem. C* **2007**, *111*, 17551−17557.

https://doi.org/10.1021/acs.jpcc.1c03372
J. Phys. Chem. C 2021, 125, 11419−11431